Check for updates

ADVANCED FUNCTIONAL MATERIALS
www.afm-journal.de

Ultrafast Carbothermal Shock Synthesis of Wadsley–Roth Phase Niobium-Based Oxides for Fast-Charging Lithium-Ion Batteries

Qilong Wu, Yuanhong Kang, Guanhong Chen, Jianken Chen, Minghui Chen, Wei Li, Zeheng Lv, Huiya Yang, Pengxiang Lin, Yu Qiao, Jinbao Zhao, and Yang Yang**

Wadsley–Roth phase niobium-based oxides show potential as anode candidates for fast-charging lithium-ion batteries. Traditional synthesis methods, however, usually involve a time-consuming calcination process, resulting in poor production efficiency. Herein, a novel carbothermal shock (CTS) method that enables the ultra-fast synthesis of various Wadsley–Roth phase Nb-based oxides within seconds is introduced. The extremely rapid heating rates enabled by CTS alter the reaction mechanism from a sluggish solid-state process to a swift liquid-phase assisted one and drive the chemical reactions away from equilibrium, thereby generating abundant oxygen vacancies and dislocations. Theoretical calculations reveal that oxygen vacancies significantly lower the energy barrier for Li^+ diffusion and enhance the intrinsic electronic conductivity. Moreover, dislocations help convert the surface tensile stress arising from Li^+ intercalation into compressive stress, effectively improving the structural integrity during cycling. Notably, this approach can also be applied to synthesize $LiFePO_4$ cathode materials under ambient conditions, eliminating the requirement for inert atmospheres. Consequently, the CTS-synthesized $Nb_{14}W_3O_{44}$||$LiFePO_4$ battery demonstrates reversible structural evolution validated by in situ XRD and exceptional cycling ability (e.g., 0.0065% capacity decay per cycle at 4 A g^{-1} over 3000 cycles). Importantly, the $Nb_{14}W_3O_{44}$||$LiFePO_4$ configuration also shows enhanced thermal stability in the Ah-level pouch cell nail penetration test, confirming its feasibility.

1. Introduction

Although the driving range of electric vehicles has now exceeded 500 km, range anxiety—largely due to extended charging times of over an hour—remains a significant barrier to their broader adoption. The solution lies in developing next-generation lithium-ion batteries (LIBs) that combine high power density with rapid charging capabilities.[1] Unfortunately, traditional carbon-based anode materials, such as graphite, fall short of meeting the demands of fast charging for several reasons. The lithiation potential of graphite is predominantly below 0.1 V (vs Li^+/Li), leading to issues such as lithium plating and solid-electrolyte interface (SEI) degradation during high-rate cycling. These issues elevate the risk of thermal runaway and pose significant safety concerns.[2–8] Additionally, the inherently slow Li^+ ion diffusion kinetics in graphite further limits its rate performance.[9,10] Therefore, there is a pressing need to develop alternative anode materials that offer both higher lithiation potentials and faster Li^+ ion diffusion coefficients, without sacrificing capacity or cycling stability.

Recently, Wadsley–Roth phases have garnered significant attention as potential anode candidates for high-rate lithium-ion batteries (LIBs), owing to their distinctive open-framework crystalline structures, multi-electron transfer capabilities (≥2 per metal atom), and a stable lithiation potential range of 1.0–1.5 V (vs Li^+/Li).[11,12] These phases are prevalent in a broad family of Nb-based complex oxides, found in both Nb_2O_5-TiO_2 and Nb_2O_5-WO_3 phase diagrams, which comprises ReO_3-like rectangular blocks made up of n × m corner-sharing MO_6 octahedra. Adjacent blocks are connected together either by edge-sharing and corner-sharing tetrahedral or octahedral sites, forming the so-called crystallographic shear structures.[13] Kocer and Griffith et al.[14,15] demonstrated that the 3D-interconnected tunnels in these Nb-based oxides act as efficient pathways for rapid Li^+ diffusion, effectively mitigating the risks of channel blocking at high currents. Moreover, the absence of local structural distortions during the lithiation process leads to lattice contraction along the block planes, effectively buffering unit cell volume expansion due to Li^+ intercalation. These attributes suggest promising applications as high-rate electrode materials.

Q. Wu, Y. Kang, G. Chen, J. Chen, M. Chen, W. Li, Z. Lv, H. Yang, P. Lin, Y. Qiao, J. Zhao, Y. Yang
College of Chemistry and Chemical Engineering
State-Province Joint Engineering Laboratory of Power Source Technology for New Energy Vehicle
Tan Kah Kee Innovation Laboratory (IKKEM)
State Key Laboratory of Physical Chemistry of Solid Surfaces
Xiamen University
Xiamen 361005, P. R. China
E-mail: jbzhao@xmu.edu.cn; yangyang419@xmu.edu.cn

The ORCID identification number(s) for the author(s) of this article can be found under https://doi.org/10.1002/adfm.202315248

DOI: 10.1002/adfm.202315248

 © 2024 Wiley-VCH GmbH

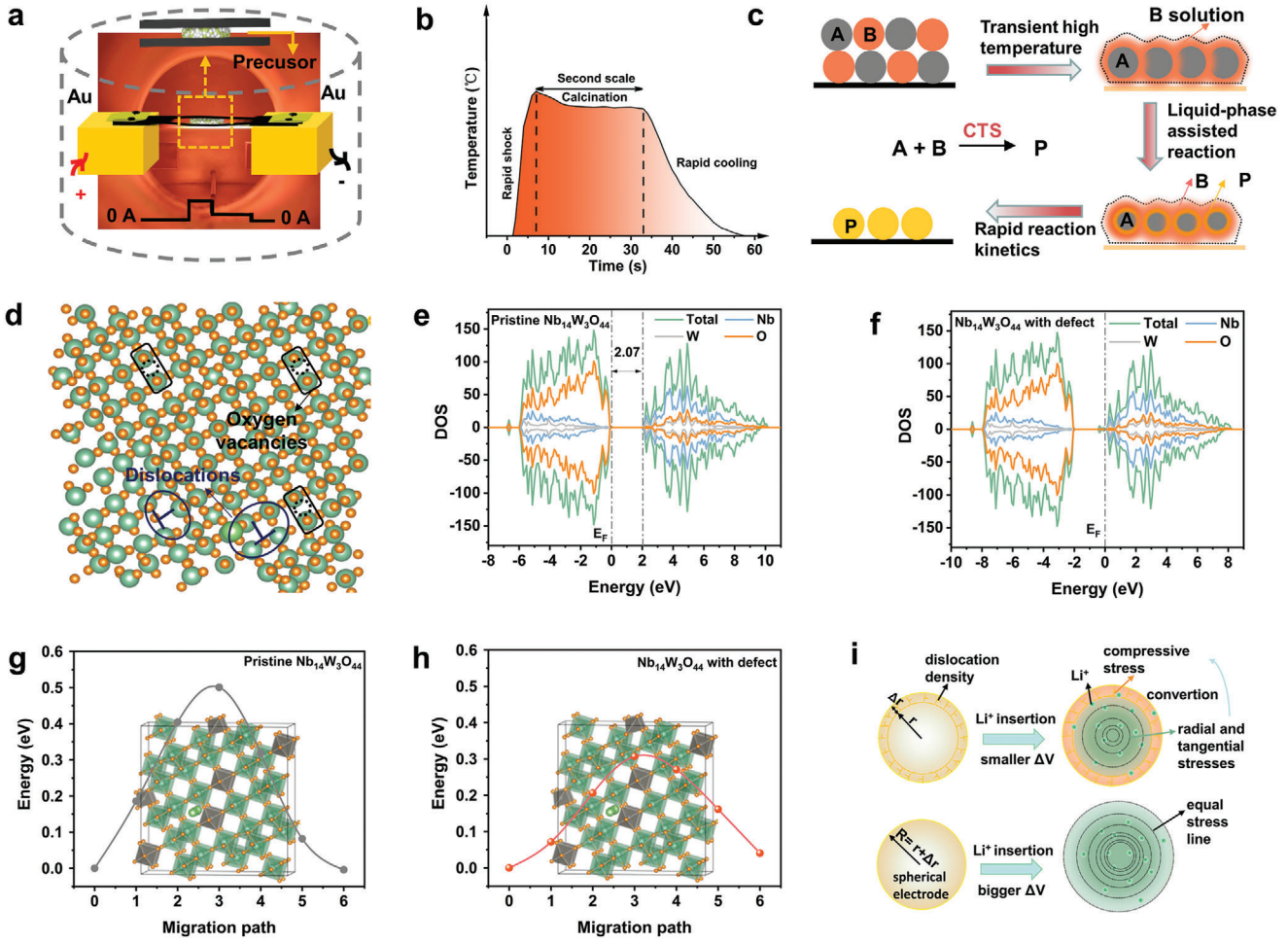

Figure 1. a) Schematic diagram of the main structure inside the Joule heating device and the picture during CTS. b) Variation of temperature with time during CTS. c) The statement of solid-state reaction to liquid-phase assisted reaction mechanism by CTS. d) Schematic of oxygen vacancies and dislocations. DOS (density of states) of e) pristine $Nb_{14}W_3O_{44}$ and f) $Nb_{14}W_3O_{44}$ with defect. Lithium-ion diffusion energy barriers of g) pristine $Nb_{14}W_3O_{44}$ and h) $Nb_{14}W_3O_{44}$ with defect (insert: picture of Li^+ diffusion behavior perpendicular to the c-axis, which is recognized as the most probable diffusion path in the material). i) Stress and volume variation (ΔV) diagrams of spherical electrodes with dislocations (upper image) and without dislocations (lower image) after Li^+ insertion. A higher density of equal stress line represents higher radical and tangential stresses.

To date, a variety of synthesis techniques, such as solid-state reactions,[16–18] sol-gel processes,[19] spray drying,[20] electrospinning,[21] and hydrothermal methods,[22] have been effectively employed to fabricate these materials. Nevertheless, these approaches almost invariably necessitate a prolonged annealing process—lasting from several hours to days—to yield well-crystallized particles. This significantly compromises production efficiency and escalates energy costs.[23,24] For example, in solid-state reactions, which involve heating a blend of powdered reactants for extended durations, the intrinsic sluggishness of atomic or ionic diffusion within or between solid particles becomes a bottleneck. Although higher temperatures can facilitate increased diffusion rates, such temperatures must generally be constrained to ≈0.7–0.8 times the melting point of the reactants (T_m), owing to container limitations (typically Pt or Al_2O_3) and concerns about particle sintering at excessive temperatures.[25] Extensive efforts have been made in the past to reduce the synthesis time and cost of materials, including methods such as microwave synthesis,[26] spark plasma synthesis,[27] and flash synthesis.[28] While these approaches have improved reaction kinetics and decreased synthesis time, it remains challenging to conduct parallel experiments with multiple compositions in a simple and high-throughput manner.[23] The carbothermal shock (CTS) technology has recently been applied to straightforward and ultrafast synthesis of high-entropy-alloy nanoparticles, high-entropy oxide nanoparticles, solid-state electrolytes, etc.[23,29–31] Hence, the CTS technology is promising for the synthesis of Nb-based oxides.

In this work, we propose a carbothermal shock (CTS) strategy for the rapid synthesis of Wadsley–Roth phase Nb-based oxides (e.g., $Nb_{14}W_3O_{44}$, $TiNb_2O_7$, $Ti_2Nb_{10}O_{29}$, $TiNb_{24}O_{62}$ and $AlNb_{11}O_{29}$) and commercial cathode materials such as $LiFePO_4$ and $LiMn_2O_4$ for fast charging LIBs, all achievable within 30 s (as shown in **Figure 1a**; Figure S1, Supporting Information). The extremely high heating rates of 104–105 K min^{-1} establish a transient high-temperature environment reaching the melting point

© 2024 Wiley-VCH GmbH

16163028, 0, Downloaded from https://onlinelibrary.wiley.com/doi/10.1002/adfm.202315248 by Xiamen University, Wiley Online Library on [18/02/2024]. See the Terms and Conditions (https://onlinelibrary.wiley.com/terms-and-conditions) on Wiley Online Library for rules of use; OA articles are governed by the applicable Creative Commons License

of Nb_2O_5 (1485 °C), transforming the otherwise sluggish solid-state reactions into liquid-phase assisted mechanisms, effectively lowering the Gibbs free energy (ΔG). Moreover, the ultra-fast cooling rate (103–104 K min^{-1}) offered by CTS technology mitigates the particle sintering issues typically triggered by the highly reactive Nb_2O_5 liquid phase.[32,33] Unexpectedly, the CTS strategy, which departs from equilibrium processes, tends to generate both point defects (oxygen vacancies) and line defects (dislocations) in Nb-based oxides.[34–37] Furthermore, $LiFePO_4$ can be also synthesized rapidly in an ambient atmosphere using the CTS approach, courtesy of a localized reducing environment provided by carbon plates and glucose, thereby eliminating the need for inert atmospheres. Most crucially, the electrochemical and safety performance of various Wadsley–Roth phase Nb-based oxides were systematically assessed by assembling lithium-ion full batteries coupled with $LiFePO_4$ cathodes, providing useful guidelines for the route selection of next-generation fast-charging LIBs.

2. Results and Discussion

The CTS method was developed to realize the one-step and ultra-fast synthesis of Wadsley–Roth phase materials by using relevant MO_x oxides (where M represents elements such as Nb, W, Ti, and Al) as precursors. Typically, precursor pellets are situated between two conductive carbon plates and then exposed to a rapid thermal shock in a reaction chamber. This entire process, including the stages of shock, thermostatic calcination, and rapid cooling, is executed in an impressively short span of ≤30 s (unless stated otherwise, this refers to the time of thermostatic calcination in this work), as depicted in Figure 1b.[38–40] A defining characteristic of the CTS method is its utilization of a shock temperature that approaches the melting point of Nb_2O_5 (1485 °C). Such an elevated temperature enables a radical shift from the conventional sluggish solid-state reactions to the swift liquid-phase assisted reactions, illustrated in Figure 1c. Accordingly, the contact area between reactants is greatly increased, leading to elevated levels of disorder within the system. This facilitates the diffusion of atoms or ions, a pivotal factor determining the rate of reactions involving solid phases.[41]

The CTS method, intriguingly, not only streamlines the synthesis process but also introduces a far-equilibrium reaction mechanism.[31] This unique mechanism results in the generation of oxygen vacancies and dislocations (Figure 1d), which may have positive effects on electrochemical performance.[34,42] Illustrating with $Nb_{14}W_3O_{44}$ as a representative case: The pristine $Nb_{14}W_3O_{44}$ possesses a bandgap ≈2.07 eV, confirming its semiconductor characteristics (Figure 1e). However, when oxygen defects are incorporated into $Nb_{14}W_3O_{44}$, there is a discernible shift of the Fermi level from the valence band to the conduction band, signifying the enhancement of electronic conductivity (Figure 1f). Furthermore, the Li^+ diffusion energy barrier of $Nb_{14}W_3O_{44}$ with defect (0.31 eV) is also calculated to be smaller than that of pristine $Nb_{14}W_3O_{44}$ (0.50 eV), demonstrating that the presence of oxygen vacancies may promote Li^+ diffusion by reducing the interaction between intercalated Li^+ and M–O framework (Figure 1g,h). Compared with oxygen vacancy, the dislocation belongs to a representative 2D defect, which is hard to be generate through traditional synthesis routes. There's existing literature that emphasizes the role of these dislocations in influencing diffusion-induced stress, as conveyed in Equation (1):[43]

$$\frac{\sigma_\zeta(r,t)}{M\chi b\mu\sqrt{\beta I/DF}\boldsymbol{b}} = \begin{pmatrix} \kappa + \frac{2}{\kappa^2}\sum_{n=1}^{\infty}\frac{\sin(\alpha_n\kappa)}{\alpha_n^2\sin(\alpha_n)}\exp\left(-\alpha_n^2\lambda\right) - \\ \frac{2}{\kappa}\sum_{n=1}^{\infty}\frac{\cos(\alpha_n\kappa)}{\alpha_n\sin(\alpha_n)}\exp\left(-\alpha_n^2\lambda\right) \end{pmatrix}^{0.5} \quad (1)$$

where σ_ζ is dislocation-induced stress, t is time, υ is Poisson's ratio, r is the distance from the center of the particle to the dislocation, D is diffusion coefficient, $\lambda = Dt/R^2$, R is the radius of particle, M is the Taylor orientation factor, F is Faraday's constant, χ is the empirical constant and μ is the shear modulus, β is a solute lattice contraction coefficient, $\boldsymbol{b}$ denotes the magnitude of the Burgers vector of the dislocation, I is constant current density, α_n ($n = 1\ 2, 3...$) are the positive roots of $\tan(\alpha_n) = \alpha_n$ and $\kappa = r/R$. It is deduced that the existence of dislocations converts part of the radial and tangential tensile stress into compressive stress (Figure 1i), which effectively reduces the possibility of electrode cracking caused by tensile stress during cycling.

The intrinsic reaction mechanism of the CTS method was further studied by XRD (X-ray diffraction) characterizations (**Figure 2a**). When the precursor was shocked to ≈1200 or 1300 °C, followed by a short calcination at ≈1200 °C for 30 s (which aligns with the temperatures typically associated with conventional solid-state reaction methods),[44] strong diffraction peaks of Nb_2O_5 and WO_3 are still detected and negligible $Nb_{14}W_3O_{44}$ phase is produced. However, a significant transition occurs when the shock temperature surges to ≈1600 °C, a value exceeding the melting point of Nb_2O_5 (1485 °C). In such a condition, after calcination at ≈1200 °C for 30 s, well-dispersed $Nb_{14}W_3O_{44}$ particles ranging from 0.5 to 1 μm (Figure 2c) are generated and no diffraction peaks of precursors are observed, which underscores the efficacy of high transient temperatures in fostering the formation $Nb_{14}W_3O_{44}$. Besides, the Raman spectroscopy also demonstrates the successful synthesis of $Nb_{14}W_3O_{44}$ without impurities (Figure S2, Supporting Information). The crystalline structure of as-prepared $Nb_{14}W_3O_{44}$ is refined to be tetragonal I-4 with high crystallinity (Figure 2b; Table S1, and Figure S3, Supporting Information). As shown in the HR-TEM (high-resolution transmission electron microscopy) image (Figure 2e), 3 × 3 light dots can be distinguished clearly, corresponding to the internal block cavities (regions with the lower electron density). Meanwhile, the clear and rhombus symmetry dots are exhibited in the SAED (selected area electron diffraction) pattern (inset in Figure 2e), revealing the single crystalline nature of the primary particles. Moreover, a large number of dislocations can be observed in the inverse fast Fourier transform (IFFT) image (Figure 2f). XPS (X-ray photoelectron spectroscopy) was further utilized to investigate the chemical environment of CTS-synthesized $Nb_{14}W_3O_{44}$, and $Nb_{14}W_3O_{44}$ prepared by the traditional solid-state method (T-$Nb_{14}W_3O_{44}$) was also used for comparison. For the O 1s XPS spectrum (Figure 2d), the strong peak at 530.1 eV belongs to the M—O bond (M stands for Nb or W atom), and the broad peak between 532 and 534 eV is associated with oxygen vacancies.[45] Obviously, the higher peak intensity observed in the CTS-synthesized $Nb_{14}W_3O_{44}$ confirms the presence of considerable oxygen vacancies. The shift of M—O band

© 2024 Wiley-VCH GmbH

16163028, 0, Downloaded from https://onlinelibrary.wiley.com/doi/10.1002/adfm.202315248 by Xiamen University, Wiley Online Library on [18/02/2024]. See the Terms and Conditions (https://onlinelibrary.wiley.com/terms-and-conditions) on Wiley Online Library for rules of use; OA articles are governed by the applicable Creative Commons License

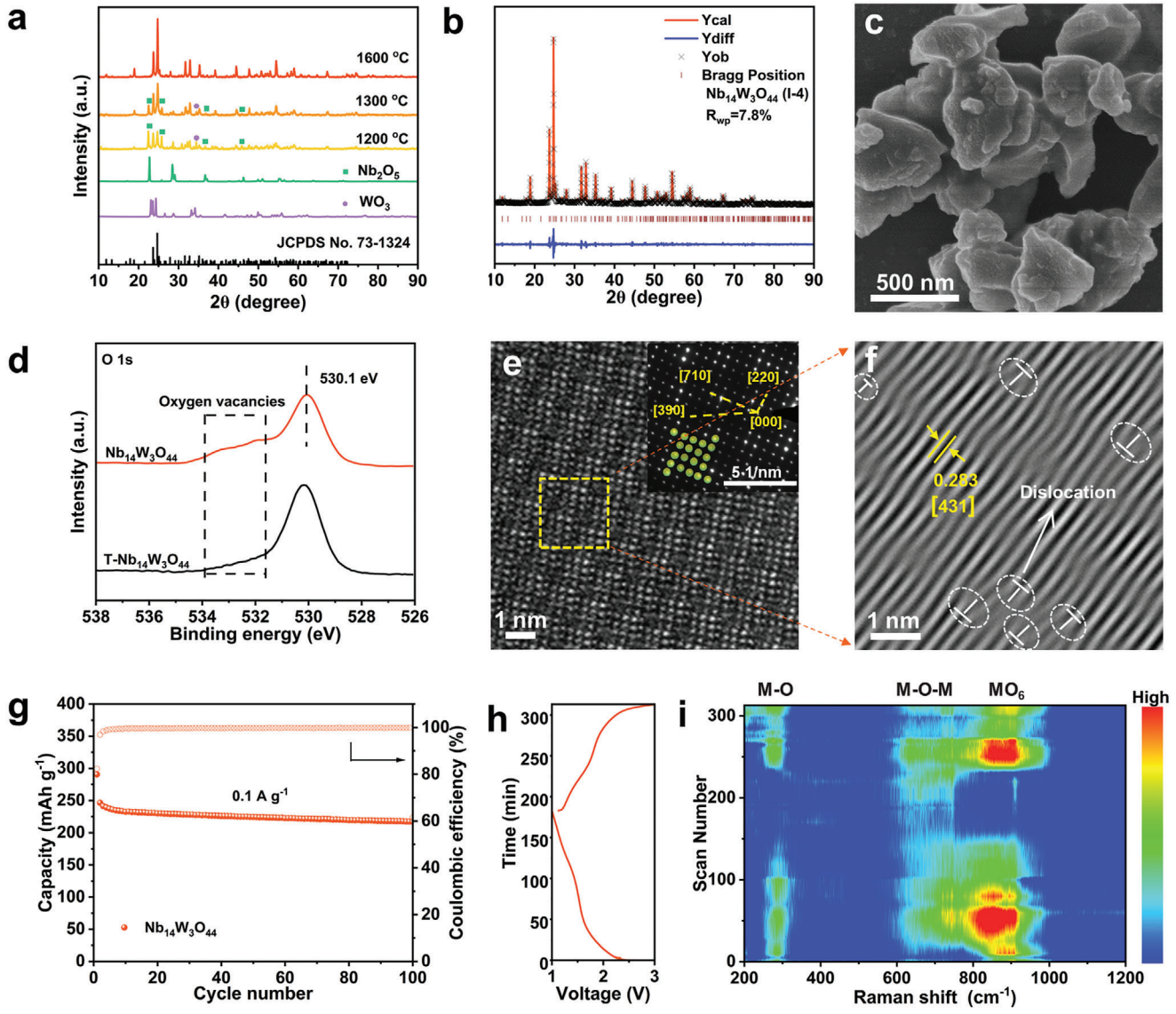

Figure 2. a) XRD peaks of the products after shocking to different temperatures and calcined at the same temperature of ≈1200 °C for 30 s. b) Refined XRD patterns for $Nb_{14}W_3O_{44}$. c) SEM image of $Nb_{14}W_3O_{44}$. d) O 1s XPS spectra of $Nb_{14}W_3O_{44}$ and T-$Nb_{14}W_3O_{44}$. e) HR-TEM image and f) the corresponding inverse fast Fourier transform (IFFT) image of $Nb_{14}W_3O_{44}$ (inset is the SAED patterns of $Nb_{14}W_3O_{44}$ and the yellow circles represent the W or Nb atom). g) Cycling performance of $Nb_{14}W_3O_{44}$ at 0.1 A g^{-1}. h) The initial discharge/charge curves at 0.1 A g^{-1} and i) its real-time Raman contour map.

toward smaller binding energies also corroborates the existence of oxygen defects (Figure S4, Supporting Information).

To evaluate Li^+ storage properties of CTS-synthesized $Nb_{14}W_3O_{44}$ anode material, various electrochemical measurements were performed in the voltage range of 1–3 V (vs Li^+/Li). The $Nb_{14}W_3O_{44}$ delivers a high initial discharge capacity of 290.6 mAh g^{-1} at 0.1 A g^{-1} with an average discharge plateau of ≈1.6 V (Figure S5, Supporting Information), and the corresponding long-term cycling performance shows 90.0% capacity retention after 100 cycles (Figure 2g). When the current density rises to 2 A g^{-1} (≈10 C), the $Nb_{14}W_3O_{44}$ exhibits an ultra-high initial capacity of 170.9 mAh g^{-1} with 87.6% capacity retention after 1000 cycles (Figure S6, Supporting Information). Even at 4 A g^{-1} (≈20 C), an outstanding initial capacity of 143.5 mAh g^{-1} with an ultra-high capacity retention of 95.9% after 1000 cycles can still be obtained (Figure S7, Supporting Information), which is superior to many previously reported $Nb_{14}W_3O_{44}$ anodes.[46–48]

The notable electrochemical performance of $Nb_{14}W_3O_{44}$ may be attributed to the fast electrochemical kinetics, which is derived from the synergistic effects of the unique open framework, oxygen vacancies, and dislocations. Therefore, the GITT (galvanostatic intermittent titration technology) and EIS (electrochemical impedance spectra) measurements were performed. The GITT images (Figure S8, Supporting Information) show that CTS-synthesized $Nb_{14}W_3O_{44}$ exhibit a comparable Li^+ diffusion coefficient (D_{Li+}) of $10^{-9.5}$–$10^{-10.5}$ cm^2 s^{-1} compared with previously

© 2024 Wiley-VCH GmbH

16163028, 0, Downloaded from https://onlinelibrary.wiley.com/doi/10.1002/adfm.202315248 by Xiamen University, Wiley Online Library on [18/02/2024]. See the Terms and Conditions (https://onlinelibrary.wiley.com/terms-and-conditions) on Wiley Online Library for rules of use; OA articles are governed by the applicable Creative Commons License

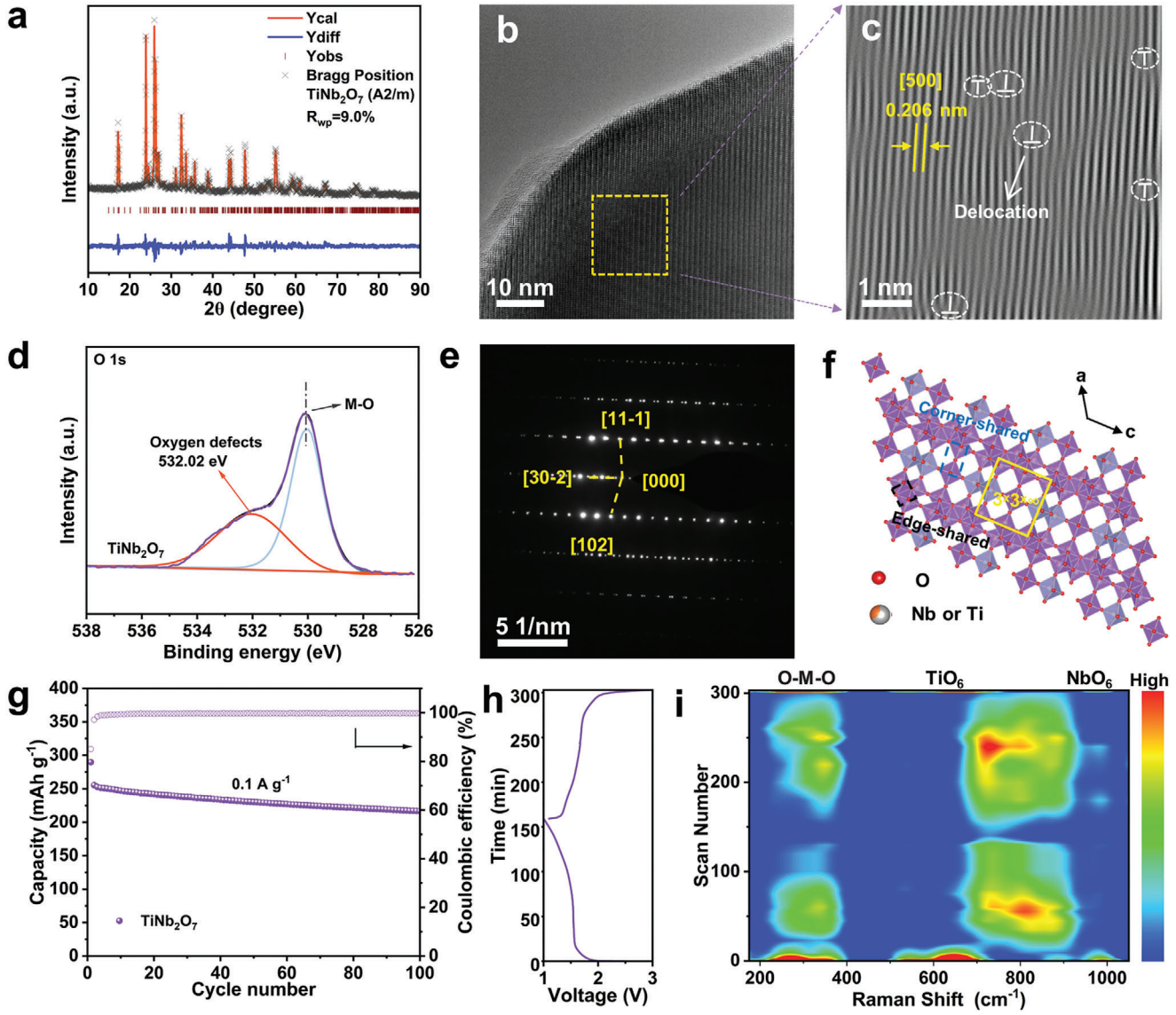

Figure 3. a) Refinement of XRD patterns for $TiNb_2O_7$. b) HR-TEM and c) the corresponding IFFT images of $TiNb_2O_7$. d) O 1s XPS spectra of $TiNb_2O_7$. e) SAED patterns of $TiNb_2O_7$. f) Structural illustration of $TiNb_2O_7$ along the *b*-axis. g) Cycling performance of $TiNb_2O_7$ at 0.1 A g^{-1}. h) The initial discharge/charge curves at 0.1 A g^{-1} and i) its real-time Raman contour map (M stands for metal atoms distributed statistically).

reported $Nb_{14}W_3O_{44}$ materials.[49,50] And the charge-transfer resistance (R_{ct}) of CTS-synthesized $Nb_{14}W_3O_{44}$ is significantly smaller than that of pristine $Nb_{14}W_3O_{44}$ (Figure S9, Supporting Information). In addition, the powder electronic conductivity tests were measured at 4.0 MPa pressure (Table S2, Supporting Information). The CTS-synthesized $Nb_{14}W_3O_{44}$ exhibits a higher electronic conductivity than pristine $Nb_{14}W_3O_{44}$. Moreover, in situ Raman testing was utilized to investigate the structural evolution of the $Nb_{14}W_3O_{44}$ anode during cycling (Figure 2h,i). The peaks located at 258.7 and 632.4 cm^{-1} are related to the M—O bond and M—O—M bond, respectively, while the other peaks located at 859.8 and 975.8 cm^{-1} stand for MO_6 octahedral structure which are associated with highest valence states of Nb^{5+} and W^{6+} (M stands for Nb or W atom).[50] Obviously, during the charging and discharging process, the peaks belonging to M—O, M—O—M and MO_6 bonds show relatively reversible location and intensity variation, which indicates that the $Nb_{14}W_3O_{44}$ anode undergoes reversible phase transition and electrochemical conversion of Nb^{5+}/Nb^{4+}, Nb^{3+} and W^{6+}/W^{5+}, W^{4+} couples during the process of (de)lithiation, demonstrating the structural stability of the $Nb_{14}W_3O_{44}$ anode material. Consequently, the CTS technique is capable of producing high-rate and structurally stable $Nb_{14}W_3O_{44}$ anode materials for fast-charging LIBs.

The CTS method is also applied to synthesize $TiNb_2O_7$, which belongs to the TiO_2-Nb_2O_5 family of Wadsley–Roth phase. Through the comprehensive measurements of XRD (**Figure 3a**; Table S3, Supporting Information), SEM (Figure S10, Supporting Information), TEM (Figure 3b,c,e), and XPS (Figure 3d), $TiNb_2O_7$ particles with the size of 500–800 nm are well-crystallized, which also possesses oxygen vacancies and dislocations. As shown in

© 2024 Wiley-VCH GmbH

16163028, 0, Downloaded from https://onlinelibrary.wiley.com/doi/10.1002/adfm.202315248 by Xiamen University, Wiley Online Library on [18/02/2024]. See the Terms and Conditions (https://onlinelibrary.wiley.com/terms-and-conditions) on Wiley Online Library for rules of use; OA articles are governed by the applicable Creative Commons License

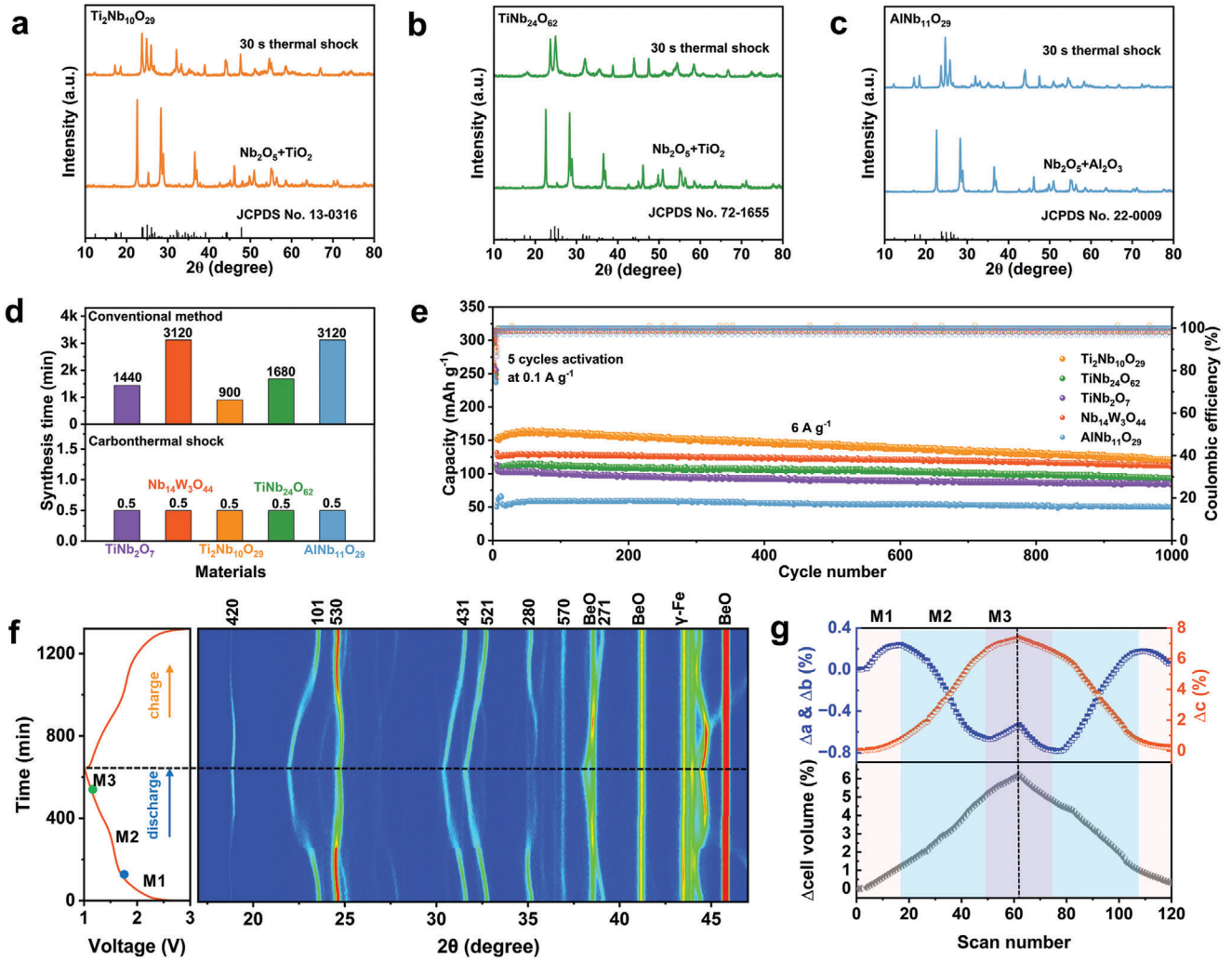

Figure 4. a–c) Ex situ XRD patterns of the $Ti_2Nb_{10}O_{29}$, $TiNb_{24}O_{62}$, and $AlNb_{11}O_{29}$. d) Comparison of the synthesis times of Wadsley–Roth anode materials by CTS and conventional approaches. e) Long-term cycling performance of $Nb_{14}W_3O_{44}$, $TiNb_2O_7$, $Ti_2Nb_{10}O_{29}$, $TiNb_{24}O_{62}$, and $AlNb_{11}O_{29}$ at 6 A g^{-1}. f) The initial discharge/charge curves along with the corresponding in situ XRD patterns of the $Nb_{14}W_3O_{44}$. g) The evolution of the refined lattice parameters and unit cell volume for the $Nb_{14}W_3O_{44}$ during different lithiation states.

Figure 3f, $TiNb_2O_7$ features blocks of size 3 × 3 with four cavities in each block. And the powder electrical conductivity of CTS-synthesized $TiNb_2O_7$ (4.8×10^{-4} S cm^{-1}) is also superior to that of pristine $TiNb_2O_7$ (7.3×10^{-5} S cm^{-1}) (Table S4, Supporting Information). Owing to the unique structure features of $TiNb_2O_7$, an outstanding power performance and cycling stability can be obtained, including a high initial discharge capacity of 335.3 mAh g^{-1} with 87.3% capacity retention at 0.1 A g^{-1} over 100 cycles and a remarkable initial capacity of 120.1 mAh g^{-1} with 85.1% capacity retention at a higher current density of 4 A g^{-1} (≈20 C) after 1000 cycles (Figure 2g; Figures S11 and S12, Supporting Information). In situ Raman measurement was also performed on $TiNb_2O_7$ electrodes to experimentally explore the evolving electrochemical interphase over time during cycling (Figure 3h,i; Figure S13, Supporting Information). The peaks at 270.1 and 169.1 cm^{-1} are attributed to the antisymmetric and symmetric bending vibrations of O—Nb—O and O—Ti—O. Another four peaks at 539.2, 650.4, 890.9, and 990.0 cm^{-1} are associated with the edge vibration of TiO_6 and NbO_6 octahedron, which is related to the highest valence states of metal atoms (Ti^{4+} and Nb^{5+}).[51,52] During the process of charging and discharging, a noticeable reversible shift of these typical peaks located at 270.1, 539.2, 650.4, 890.9, and 990.0 cm^{-1} can be observed, revealing that the host structure of $TiNb_2O_7$ is well reserved.

To demonstrate the universality of CTS for the fabrication of Wadsley–Roth phases, other Nb-based oxides, including $Ti_2Nb_{10}O_{29}$, $TiNb_{24}O_{62}$, and $AlNb_{11}O_{29}$, were also tried. Similar to $Nb_{14}W_3O_{44}$ and $TiNb_2O_7$ mentioned above, these Wadsley–Roth phase materials can also be successfully synthesized with high crystallinity and irregular-shaped nanoscale particles (**Figure 4**a–c; Figure S14, Supporting Information). Taking $Ti_2Nb_{10}O_{29}$ as a representative material to further investigate its micromorphology and chemical properties. The HR-TEM image shows clear lattice stripes of 0.374 nm, belonging to the [011] plane of the orthorhombic $Ti_2Nb_{10}O_{29}$ (Figure S15, Supporting Information). In addition, it is noted that a large number of

© 2024 Wiley-VCH GmbH

16163028, 0, Downloaded from https://onlinelibrary.wiley.com/doi/10.1002/adfm.202315248 by Xiamen University, Wiley Online Library on [18/02/2024]. See the Terms and Conditions (https://onlinelibrary.wiley.com/terms-and-conditions) on Wiley Online Library for rules of use; OA articles are governed by the applicable Creative Commons License

dislocations and oxygen vacancies presenting in $Ti_2Nb_{10}O_{29}$ were also confirmed by IFFT and XPS (Figures S16 and S17, Supporting Information). Encouragingly, it is verified that the time required to prepare Wadsley–Roth anode materials for fast-charging LIBs by CTS is less than 1 min, which is almost negligible when compared to traditional methods (Figure 4d).[46,53–56]

Reversible capacities of 233.0, 213.2, and 197.4 mAh g^{-1} can be retained after 100 cycles at 0.1 A g^{-1} for $Ti_2Nb_{10}O_{29}$, $TiNb_{24}O_{62}$, and $AlNb_{11}O_{29}$, respectively (Figure S18, Supporting Information). The corresponding dQ/dV curves show their safe lithiation voltage of >1.5 V (much higher than Li^+ plating potential) and small polarization voltage of <0.1 V (Figure S19, Supporting Information). The D_{Li+} of these three CTS-synthesized Wadsley–Roth phases obtained from GITT tests are ≈10^{-11} to 10^{-9} cm^2 s^{-1} (Figures S8 and S20, Supporting Information), comparable to those samples prepared by other conventional methods.[21,3,57,58] To further investigate the high-rate and durable capability of CTS-synthesized materials, long-term cycle performance was also investigated at an extremely high current density of 6 A g^{-1} (≈30 C, meaning a battery can be recharged in ≈2 min, Figure 4e). The fast-charging capacity of niobium-based oxides prepared by CTS method also possesses noticeable advantages compared with the material prepared by other methods (Table S5, Supporting Information). Taking into account both cycling stability and reversible capacity, $Nb_{14}W_3O_{44}$ seems to be a preferred choice (111.7 mAh g^{-1} with a high capacity retention of 89.3% after 1000 cycles).

In situ XRD of $Nb_{14}W_3O_{44}$, $TiNb_2O_7$, and $Ti_2Nb_{10}O_{29}$ were conducted to further reveal their structural evolution induced by Li^+ insertion. As can be seen in the counterplot (Figure 4f), all peaks of $Nb_{14}W_3O_{44}$ evolve smoothly and return to their original position after the initial cycle. Additionally, no emerging features were observed throughout the cycle. These results reveal that the $Nb_{14}W_3O_{44}$ undergoes a reversible solid-solution reaction during the charging and discharging process. Furthermore, the lattice parameters of $Nb_{14}W_3O_{44}$ in different lithiated states were obtained by refinement. For the $Nb_{14}W_3O_{44}$ (Figure 4g), during the initial discharge (M1 region), all lattice parameters of a, b, and c expand simultaneously, corresponding to a voltage range of ≈3.0–≈1.7 V, demonstrating that $Nb_{14}W_3O_{44}$ can allow a small amount of Li^+ to be embedded in the bulk phase without changing the bonding and electronic structure. With further embedded Li^+ (M2 region), the *c*-axis continues to increase, while the *ab*-axis shrinks, indicating that the Li^+ may diffuse along the *c*-axis. The simultaneous monotonic increase of *c*-axis and volume can also illustrate this conclusion. The unexpected contraction of ab plan in the M2 region can be attributed to the Coulombic interaction between Li^+ and O^{2-}. When the voltage is discharged from ≈1.3 to ≈1.0 V (M3 region), all the a, b, and c axes further expand, which may be related to the larger ionic radius of the discharge end state. Finally, its unit-cell volume increased by 6.2% at the end of the discharge. The structural evolution of $TiNb_2O_7$ and $Ti_2Nb_{10}O_{29}$ is similar to that of $Nb_{14}W_3O_{44}$, indicating that they also have highly reversible structures (Figures S21 and S22, Supporting Information). However, the volume variation of $TiNb_2O_7$ (9.4%) and $Ti_2Nb_{10}O_{29}$ (8.4%) in the full lithiation state is larger than that of $Nb_{14}W_3O_{44}$ (Table S6), which may be related to the fact that $TiNb_2O_7$ and $Ti_2Nb_{10}O_{29}$ have worse cycling stability than $Nb_{14}W_3O_{44}$. Therefore, CTS method has been demonstrated to be a powerful strategy for realizing ultra-fast production of various Wadsley–Roth phase anode materials with excellent fast-charging capability.

In order to fabricate practical fast-charging LIBs, an appropriate cathode is also indispensable. Therefore, the possibility of using the CTS technology to synthesize commercial cathode materials has been also explored. It is encouraging that the in situ preparation of $LiFePO_4$ is realized in 20 s even in the air atmosphere (**Figure 5**a,b), eliminating the utilization of an inert atmosphere of conventional methods. The precursor is a simple mixture of iron phosphate, lithium carbonate, and glucose. Which glucose serves as a reaction templating agent and reducing agent, which not only reduces primary particle sintering but also works together with the carbon plate's own reducing properties under high-temperature conditions to form the local strong reducing atmosphere around the precursor. Thus, when the precursor was shocked to ≈750 °C, Fe^{3+} presenting in the precursor will be quickly reduced to Fe^{2+}, which ensures the generation of $LiFePO_4$ cathode material.

Consequently, a pure orthogonal $LiFePO_4$ cathode with high crystallinity was successfully synthesized by CTS (Figure 5c; Table S7, Supporting Information). The SEM image shows that the average nano-sized particle of $LiFePO_4$ is smaller than the anode described above, which may be caused by the usage of the template agent and nano-sized $FePO_4$ precursor (Figure 5d). The element mapping of $LiFePO_4$ exhibits that Fe, P, and O elements are also uniformly spread (Figure 5e). The HR-TEM image (Figure 5g) shows that clearly resolved lattice fringes with interplane space of 0.367 nm are detected, corresponding to [011] planes of orthogonal $LiFePO_4$. Furthermore, the bright and periodic distribution of diffraction spots in the SAED also indicates the formation of single crystal particles (Figure 5h). The chemical valence state of $LiFePO_4$ sample was further investigated by XPS. Both the P 2p XPS spectra and Li 1s XPS spectra exhibit typical spin-orbit single state at 133.5 and 55.2 eV respectively, which could be assigned to the P^{5+} and Li^+. Additionally, as a result of spin-orbit coupling, the Fe 2p spectrum splits into Fe $2p_{3/2}$ and Fe $2p_{1/2}$, representing the main peak at 711.1 eV and the relative satellite peak at 723.6 eV, separately (Figure 5f). Actually, the appearance of shoulder or satellite peaks is typical of transition metal ions possessing partially filled d-orbits. The binding energy of these two different peaks is characteristic of the valence of Fe^{2+} in the olivine structure of $LiFePO_4$ as reported previously.[59]

Half-cells were assembled to evaluate the electrochemical performance of $LiFePO_4$ within an electrochemical window of 2.5–3.8 V (vs Li^+/Li). The resultant $LiFePO_4$ delivers a high initial discharge capacity of 154.0 mAh g^{-1} with a satisfactory capacity retention of 98.3% at 0.1 C after 100 cycles, a reversible capacity of 141.6 mAh g^{-1} with 91.2% capacity retention at 1 C after 500 cycles and an extraordinary rate capacity of 104.3 mAh g^{-1} at 10 C (Figure 5i–k; Figures S23 and S24, Supporting Information). The rate capacity is comparable to many nano-sized $LiFePO_4$ materials synthesized by complex hydrothermal and electrostatic spinning approaches (Table S8, Supporting Information). In addition to $LiFePO_4$, cubic-phase $LiMn_2O_4$ was also prepared by the CTS method, which also exhibits good electrochemical properties (Figures S25–S29, Supporting Information). The above results have strongly demonstrated the promising application prospects of CTS technology in the synthesis of cathode materials.

© 2024 Wiley-VCH GmbH

16163028, 0, Downloaded from https://onlinelibrary.wiley.com/doi/10.1002/adfm.202315248 by Xiamen University, Wiley Online Library on [18/02/2024]. See the Terms and Conditions (https://onlinelibrary.wiley.com/terms-and-conditions) on Wiley Online Library for rules of use; OA articles are governed by the applicable Creative Commons License

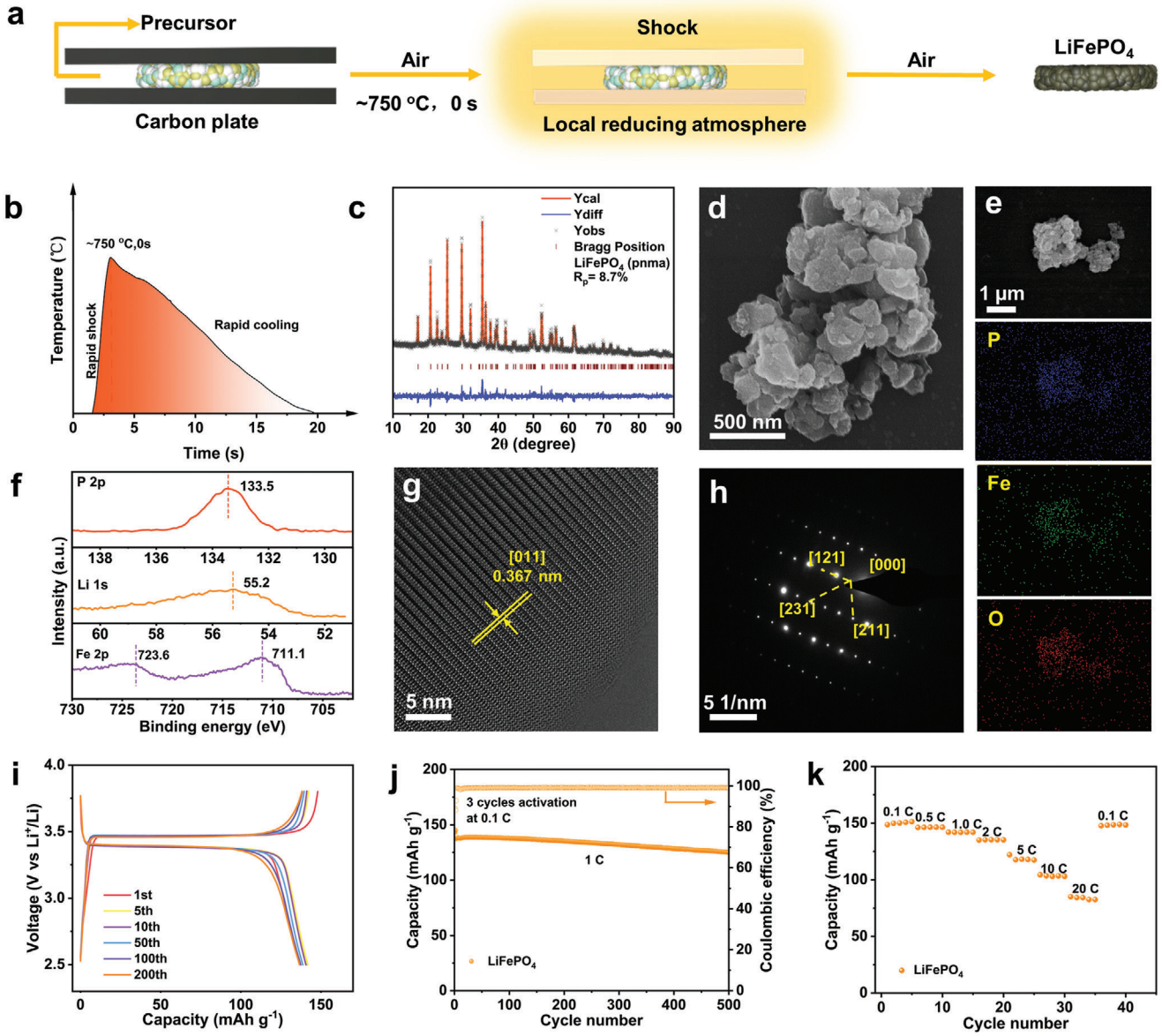

Figure 5. a) Schematic of the in situ fabrication of $LiFePO_4$. b) Temperature curve of $LiFePO_4$ prepared by CTS process. c) Refined XRD patterns of $LiFePO_4$. d) SEM image of $LiFePO_4$. e) Element mapping of $LiFePO_4$. f) P 2p, Li 1s, Fe 2p XPS spectra of $LiFePO_4$. g) HR-TEM image of $LiFePO_4$. h) SADE patterns of $LiFePO_4$. i) Typical charge/discharge profiles of $LiFePO_4$ at 1 C within 2.5–3.8 V and j) corresponding long-term cycling performance. k) Rate performance of $LiFePO_4$.

With the intention of further verifying the compatibility of the anode and cathode materials synthesized by CTS technique, $Nb_{14}W_3O_{44}$||$LiFePO_4$ and $TiNb_2O_7$||$LiFePO_4$ full cells were fabricated. The $Nb_{14}W_3O_{44}$||$LiFePO_4$ full cell has an output voltage of 1.8 V, which can easily light up a LED light with a voltage of 2 V after assembling into a pouch cell (Figure S30, Supporting Information). Similar to the results of the half-cell test, the $Nb_{14}W_3O_{44}$||$LiFePO_4$ full cells also demonstrate extraordinary electrochemical performance. As shown in Figure S31 (Supporting Information), at a relatively high current density of 2 A g^{-1} (≈10 C), the stable cycling performance of $Nb_{14}W_3O_{44}$||$LiFePO_4$ full cell is attained, and there is almost no decay in capacity from 500 to 3500 cycles. From the results of the rate performance test, the $Nb_{14}W_3O_{44}$||$LiFePO_4$ full cells also show high-power capability with relatively high capacities of 162.3, 138.3, and 109.7 mAh g^{-1} at 0.5, 1, and 2 A g^{-1}, respectively (Figure S32, Supporting Information). Impressively, at the power density of 180 W kg^{-1}, the $Nb_{14}W_3O_{44}$||$LiFePO_4$ full cell puts out the highest energy density of 133.7 Wh kg^{-1} (**Figure 6b**), which is superior compared with other high-rate anodes coupled with $LiFePO_4$ cathode.[60–63] Furthermore, the high-power performance and stability of $Nb_{14}W_3O_{44}$||$LiFePO_4$ full cells were also evaluated. Even at the current density of 4 A g^{-1} (≈20 C) (Figure 6a), the excellent capacity retention of 80.6% after 3000 cycles can still be

© 2024 Wiley-VCH GmbH

16163028, 0, Downloaded from https://onlinelibrary.wiley.com/doi/10.1002/adfm.202315248 by Xiamen University, Wiley Online Library on [18/02/2024]. See the Terms and Conditions (https://onlinelibrary.wiley.com/terms-and-conditions) on Wiley Online Library for rules of use; OA articles are governed by the applicable Creative Commons License

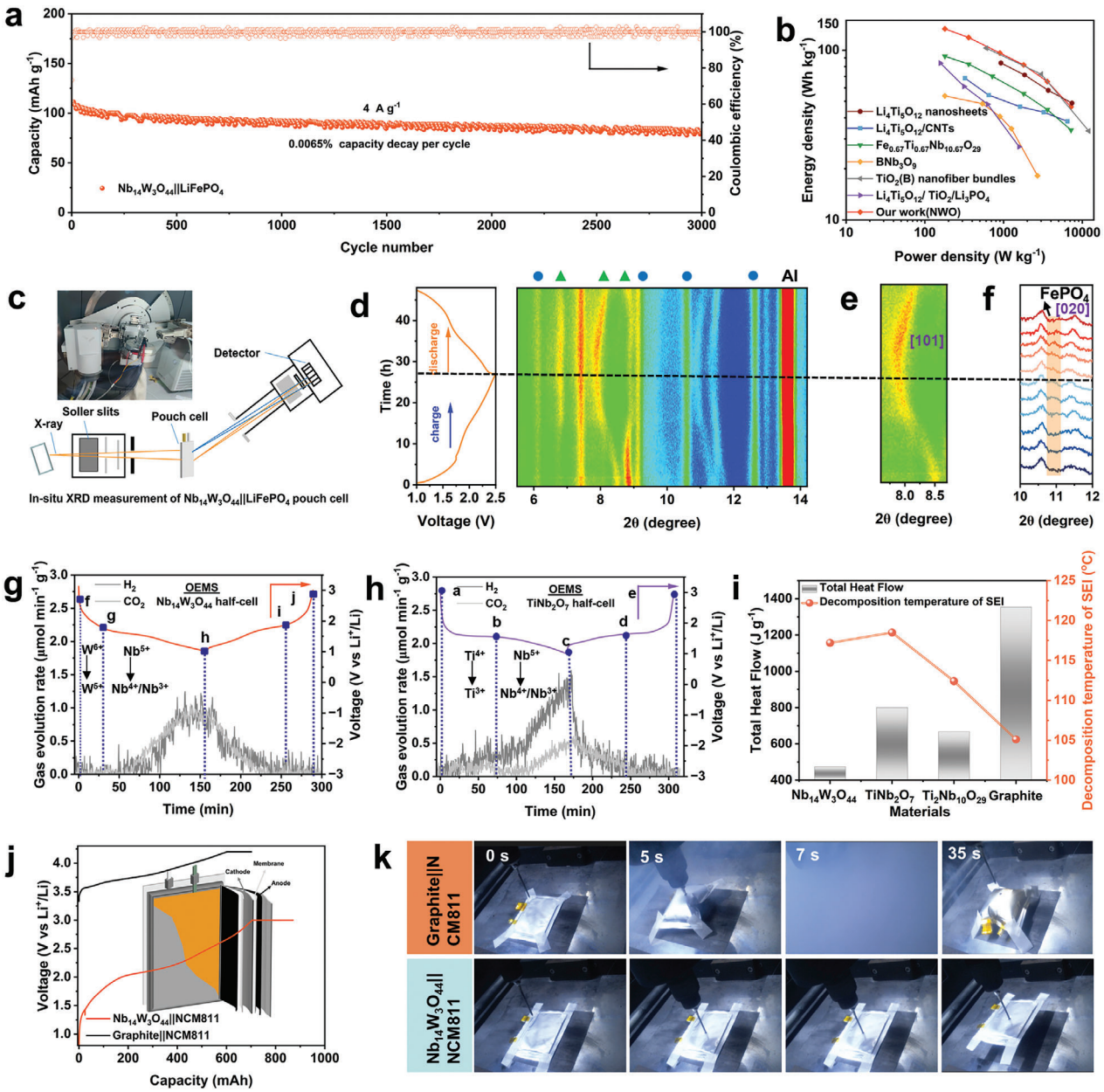

Figure 6. a) Cycling performance of $Nb_{14}W_3O_{44}$||$LiFePO_4$ full cell at 4 A g^{-1}. b) Mass energy density and power density of $Nb_{14}W_3O_{44}$||$LiFePO_4$ full cell compares to other high-power anodes with $LiFePO_4$ as a counter. c) In situ XRD schematic diagram of $Nb_{14}W_3O_{44}$||$LiFePO_4$ pouch cell. d) The initial charge/discharge curves at 10 mA g^{-1} along with the corresponding in situ XRD patterns (The blue circle represents the peak of $LiFePO_4$ and the green triangle represents the peak of $Nb_{14}W_3O_{44}$, while the remaining peaks are challenging to differentiate). e) Contour plots of the [101] Bragg peaks. f) part of XRD curves of the $Nb_{14}W_3O_{44}$||$LiFePO_4$ pouch cell within the 2θ region between 10° and 12°. OEMS results collected during the initial cycle of g) the $TiNb_2O_7$ half-cell and h) the $Nb_{14}W_3O_{44}$ half-cell (the evolution rates of H_2 and CO_2 are identified by the mass-to-charge ratio (m/z) and quantified by standard gas calibration). i) Statistics of total heating flow and decomposition temperature of SEI based on the results of DSC testing. j) The charge curves of $Nb_{14}W_3O_{44}$||$LiFePO_4$ and graphite||$LiNi_{0.8}Co_{0.1}Mn_{0.1}O_2$ (NCM811) (inset: diagram of a stacked pouch cell). k) The nail penetration test of the graphite||NCM811 and $Nb_{14}W_3O_{44}$||NCM811 pouch cells (variation of graphite||NCM811 and $Nb_{14}W_3O_{44}$||NCM811 pouch cells with time throughout the process).

performed. Moreover, the $TiNb_2O_7$||$LiFePO_4$ full cells also exhibit excellent cycling and rate performances (Figures S33 and S34, Supporting Information), further proving the fast-charging capability and applicability of both the cathode and anode materials synthesized by CTS.

The structural evolution of anode and cathode in the full cell system is rarely explored simultaneously, therefore, $Nb_{14}W_3O_{44}$||$LiFePO_4$ pouch cells were assembled for in situ XRD measurement (Figure 6c–f). From the XRD spectrum, the characteristic peaks of $Nb_{14}W_3O_{44}$ and $LiFePO_4$ can be clearly

© 2024 Wiley-VCH GmbH

16163028, 0, Downloaded from https://onlinelibrary.wiley.com/doi/10.1002/adfm.202315248 by Xiamen University, Wiley Online Library on [18/02/2024]. See the Terms and Conditions (https://onlinelibrary.wiley.com/terms-and-conditions) on Wiley Online Library for rules of use; OA articles are governed by the applicable Creative Commons License

distinguished in the 2θ angle range from 5.5° to 14.5° (Figure 6d). Similar to the in situ XRD test results of $Nb_{14}W_3O_{44}$ half cells, all diffraction peaks of $Nb_{14}W_3O_{44}$ in $Nb_{14}W_3O_{44}$||$LiFePO_4$ pouch cell evolve smoothly and no new peaks belonging to $Nb_{14}W_3O_{44}$ are observed, which is the characteristic of a single-phase reaction mechanism. However, the difference lies in the fact that in the in situ XRD test of pouch cells, the peaks of $Nb_{14}W_3O_{44}$ do not return to their initial positions completely, indicating that some embedded lithium cannot be completely extracted from $Nb_{14}W_3O_{44}$. This may be one of the reasons for the early capacity decay of $Nb_{14}W_3O_{44}$||$LiFePO_4$ full cells. The selected peak graph of [101] specifies the evolution behavior of $Nb_{14}W_3O_{44}$ (Figure 6e). During the charging and discharging process, the diffraction peak of [101] shifts from 8.52° to 8.19°, reflecting an incompletely reversible lattice evolution of $Nb_{14}W_3O_{44}$, which may be caused by excessive discharge of $Nb_{14}W_3O_{44}$. Different from the $Nb_{14}W_3O_{44}$ anode, during the charging process, a new diffraction peak belonging to $FePO_4$ is observed within the diffraction peaks of $LiFePO_4$ at 10°–12°. However, as the voltage is discharged to 1.0 V, the diffraction peak of $FePO_4$ disappears. These results reflect the $LiFePO_4$ goes through a typical two-phase reaction (Figure 6f).[64]

We carried out online electrochemical mass spectrometry (OEMS) measurements on $TiNb_2O_7$ and $Nb_{14}W_3O_{44}$ electrodes and analyzed the concentration of their real-time gas evolution process during the initial cycle (Figure 6g,h). The OEMS image of $TiNb_2O_7$ shows that during the discharge process, as Ti^{4+} is reduced to Ti^{3+}, H_2 and CO_2 are generated. Nevertheless, no such phenomenon is observed for the reduction of W^{6+} to W^{5+} in $Nb_{14}W_3O_{44}$, indicating that Ti^{3+} has a certain catalytic effect on the production of gases, which was also mentioned in $Li_4Ti_5O_{12}$ electrodes.[65,66] For both $TiNb_2O_7$ and $Nb_{14}W_3O_{44}$, as Nb^{5+} is reduced to Nb^{4+} and Nb^{3+}, the rates of gas production become more rapid, suggesting that Nb^{4+} and Nb^{3+} may have a stronger catalytic effect on the gas production. There are three main gas components detected H_2, CO_2, and CO during cycling (Table S9, Supporting Information). Considering the flammability and explosiveness, H_2 is clearly the component that has a more detrimental impact on battery safety. It can be concluded that the amount of H_2 generated on $Nb_{14}W_3O_{44}$ (85.8 μmol g^{-1}) is lower than that on $TiNb_2O_7$ (118.7 μmol g^{-1}) during the initial cycle. The thermal runaway of lithiated anodes is also one of the most significant safety factors in the practical application of LIBs and the risk of thermal runaway increases rapidly as the current rises,[40] which can be reflected by the DSC (Differential scanning calorimetric measurements) of lithiated materials and electrolyte. All DSC results of graphite, $TiNb_2O_7$, $Nb_{14}W_3O_{44}$, and $Ti_2Nb_{10}O_{29}$ show three exothermic peaks (denoted as I, II, and III), which in turn represent the decomposition reaction of SEI, the reaction between electrode material and electrolyte, and the reaction between electrode material and binder, respectively (Figure S35, Supporting Information).[67] The decomposition of SEI is generally considered to be the beginning of thermal runaway, which triggers other exothermic reactions of LIBs.[68] Obviously, as shown in Figure 6i, compared to $Ti_2Nb_{10}O_{29}$, $TiNb_2O_7$ and $Nb_{14}W_3O_{44}$, the graphite anode has the lowest SEI decomposition temperature of 105.1 °C and the highest total heat flow of 1354 J g^{-1}, indicating that all of $Ti_2Nb_{10}O_{29}$, $TiNb_2O_7$ and $Nb_{14}W_3O_{44}$ anodes are intrinsically safer than graphite anode. Furthermore, the $Nb_{14}W_3O_{44}$ anode demonstrates a more stable SEI and releases less total heat than $TiNb_2O_7$ and $Ti_2Nb_{10}O_{29}$, suggesting higher safety of $Nb_{14}W_3O_{44}$ anode. Based on the above results, the system of Nb_2O_5-WO_3 may be a better choice than Nb_2O_5-TiO_2 for fast-charging LIBs.

Finally, in order to better replicate actual conditions, $Nb_{14}W_3O_{44}$||NCM811 and graphite||NCM811 pouch cells with a charge capacity of ≈0.8 Ah were assembled for the nail penetration test, which simulates the internal short circuit of LIBs (Figure 6j,k).[69–71] When the nail pierces graphite||NCM811 pouch cell, its volume instantly expands and the tactile temperature rises violently, accompanied with a large amount of white smoke and gas coming out. However, for the $Nb_{14}W_3O_{44}$||NCM811 pouch cell, no changes were observed except for a slight increase in tactile temperature. Additionally, following the test, the $Nb_{14}W_3O_{44}$||NCM811 pouch cell still maintains an open circuit voltage of 2.402 V, which can still easily light up an LED lamp with a voltage requirement of 2 V (Figure S36, Supporting Information).

3. Conclusion

In conclusion, we have developed a universal carbothermal shock (CTS) technique that enables the synthesis of Wadsley–Roth phase anodes, including $Nb_{14}W_3O_{44}$, $TiNb_2O_7$, $Ti_2Nb_{10}O_{29}$, $TiNb_{24}O_{62}$, and $AlNb_{11}O_{29}$, as well as mainstream cathode materials such as $LiFePO_4$ and $LiMn_2O_4$, all within 30 s. The extraordinary heating rates achieved by CTS not only accelerate sluggish solid-state reactions into swift liquid-phase assisted mechanisms but also push the reactions far from equilibrium. This leads to the formation of oxygen vacancies and dislocations, which is demonstrated to significantly enhance both Li^+ and electron transport through theoretical calculations. Owing to the synergistic effects of these unique structural features, the CTS-synthesized materials show excellent fast charging capabilities. Particularly, the CTS-synthesized $Nb_{14}W_3O_{44}$||$LiFePO_4$ full cells exhibit a remarkable capacity retention of 80.6% at 4 A g^{-1} (≈20 C) over 3000 cycles. Furthermore, in situ Raman, in situ XRD, DSC, and nail penetration tests were conducted to investigate the structural reversibility and safety features of $Nb_{14}W_3O_{44}$ and $TiNb_2O_7$. A comparative study of gas production behavior reveals that $Nb_{14}W_3O_{44}$ offers better thermal stability and fast-charging capabilities than its Ti-based counterparts, suggesting that Nb_2O_5-WO_3 systems may offer advantages over Nb_2O_5-TiO_2 for fast-charging LIBs. Overall, the CTS approach offers a highly efficient route for synthesizing and modifying electrode materials, fulfilling the need for next-generation fast-charging LIBs.

Supporting Information

Supporting Information is available from the Wiley Online Library or from the author.

Acknowledgements

The authors gratefully acknowledge the financial support from the National Natural Science Foundation of China (Grant No. 22109030 and

© 2024 Wiley-VCH GmbH

16163028, 0, Downloaded from https://onlinelibrary.wiley.com/doi/10.1002/adfm.202315248 by Xiamen University, Wiley Online Library on [18/02/2024]. See the Terms and Conditions (https://onlinelibrary.wiley.com/terms-and-conditions) on Wiley Online Library for rules of use; OA articles are governed by the applicable Creative Commons License

22021001), Fundamental Research Funds for the Central Universities (Grant No.20720220073), Fujian Industrial Technology Development and Application Plan (Grant No.2022I0002), and The Key Research and Development Program of Yunnan Province (Grant No.202103AA080019). The numerical calculations in this paper have been done on Hefei advanced computing center.

Conflict of Interest

The authors declare no conflict of interest.

Data Availability Statement

The data that support the findings of this study are available from the corresponding author upon reasonable request.

Keywords

carbothermal shock, fast-charging Li-ion batteries, $LiFePO_4$, ultra-fast synthesis, Wadsly–Roth phase

Received: November 30, 2023
Revised: January 26, 2024
Published online:

[1] S. Deng, H. Zhu, G. Wang, M. Luo, S. Shen, C. Ai, L. Yang, S. Lin, Q. Zhang, L. Gu, B. Liu, Y. Zhang, Q. Liu, G. Pan, Q. Xiong, X. Wang, X. Xia, J. Tu, *Nat. Commun.* **2020**, *11*, 132.
[2] S.-S. Kim, S. M. Jung, C. Senthil, H. Y. Jung, *ACS Nano* **2021**, *15*, 18437.
[3] Y. Zhang, C. Kang, W. Zhao, B. Sun, X. Xiao, H. Huo, Y. Ma, P. Zuo, S. Lou, G. Yin, *Energy Storage Mater.* **2022**, *47*, 178.
[4] C. Yang, D. Ma, J. Yang, M. Manawan, T. Zhao, Y. Feng, J. Li, Z. Liu, Y. Zhang, R. B. Von Dreele, B. H. Toby, C. P. D. L. Albarrán, J. H. Pan, *Adv. Funct. Mater.* **2023**, *33*, 2212854.
[5] Z. Song, H. Li, W. Liu, H. Zhang, J. Yan, Y. Tang, J. Huang, H. Zhang, X. Li, *Adv. Mater.* **2020**, *32*, 2001001.
[6] Z.-S. Wu, W. Ren, L. Wen, L. Gao, J. Zhao, Z. Chen, G. Zhou, F. Li, H.-M. Cheng, *ACS Nano* **2010**, *4*, 3187.
[7] K. J. Griffith, K. M. Wiaderek, G. Cibin, L. E. Marbella, C. P. Grey, *Nature* **2018**, *559*, 556.
[8] Y. Zheng, W. Qiu, L. Wang, J. Liu, S. Chen, C. Li, *Adv. Sci.* **2022**, *9*, 2202201.
[9] Q. Fu, X. Liu, J. Hou, Y. Pu, C. Lin, L. Yang, X. Zhu, L. Hu, S. Lin, L. Luo, Y. Chen, *J. Power Sources* **2018**, *397*, 231.
[10] J. P. Pender, G. Jha, D. H. Youn, J. M. Ziegler, I. Andoni, E. J. Choi, A. Heller, B. S. Dunn, P. S. Weiss, R. M. Penner, C. B. Mullins, *ACS Nano* **2020**, *14*, 1243.
[11] R. Zhan, D. Ren, S. Liu, Z. Chen, X. Liu, W. Wang, L. Fu, X. Wang, S. Tu, Y. Ou, H. Ge, A. J. Y. Wong, Z. W. Seh, L. Wang, Y. Sun, *Adv. Energy Mater.* **2023**, *13*, 2202544.
[12] J.-T. Han, J. B. Goodenough, *Chem. Mater.* **2011**, *23*, 3404.
[13] A. A. Voskanyan, A. Navrotsky, *Annu. Rev. Mater. Res.* **2021**, *51*, 521.
[14] K. J. Griffith, I. D. Seymour, M. A. Hope, M. M. Butala, L. K. Lamontagne, M. B. Preefer, C. P. Koçer, G. Henkelman, A. J. Morris, M. J. Cliffe, S. E. Dutton, C. P. Grey, *J. Am. Chem. Soc.* **2019**, *141*, 16706.
[15] K. J. Griffith, Y. Harada, S. Egusa, R. M. Ribas, R. S. Monteiro, R. B. Von Dreele, A. K. Cheetham, R. J. Cava, C. P. Grey, J. B. Goodenough, *Chem. Mater.* **2021**, *33*, 4.
[16] J. Zheng, R. Xia, C. Sun, N. Yaqoob, Q. Qiu, L. Zhong, Y. Li, P. Kaghazchi, K. Zhao, J. E. T. Elshof, M. Huijben, *Small* **2023**, *19*, 2301967.
[17] Y. Han, M. Yang, Y. Zhang, J. Xie, D. Yin, C. Li, *Chem. Mater.* **2016**, *28*, 3139.
[18] D. Cao, Z. Yao, J. Liu, J. Zhang, C. Li, *Energy Storage Mater.* **2018**, *11*, 152.
[19] C. H. Lu, K. C. Li, S. Balaji, P. S. Kumar, *Ceram. Int.* **2021**, *47*, 18619.
[20] G. Zhu, Q. Li, Y. Zhao, R. Che, *ACS Appl. Mater. Interfaces* **2017**, *9*, 41258.
[21] T. Jiang, S. Ma, J. Deng, T. Yuan, C. Lin, M. Liu, *Adv. Sci.* **2022**, *9*, 2105119.
[22] Y. Tang, S. Deng, S. Shi, L. Wu, G. Wang, G. Pan, S. Lin, X. Xia, *Electrochim. Acta* **2020**, *332*, 135433.
[23] W. Fan, Z. Ren, Z. Sun, X. Yao, B. Yildiz, J. Li, *ACS Energy Lett.* **2022**, *7*, 1223.
[24] Y. Qiao, C. Chen, Y. Liu, Y. Liu, Q. Dong, Y. Yao, X. Wang, Y. Shao, C. Wang, L. Hu, *Nano Lett.* **2021**, *21*, 4517.
[25] T. J. Gray, *J. Am. Ceram. Soc.* **1954**, *37*, 534.
[26] M. Oghbaei, O. Mirzaee, *J. Alloys Compd.* **2010**, *494*, 175.
[27] O. Guillon, J. Gonzalez-Julian, B. Dargatz, T. Kessel, G. Schierning, J. Räthel, M. Herrmann, *Adv. Eng. Mater.* **2014**, *16*, 830.
[28] Y. Zhang, J. Nie, J. M. Chan, J. Luo, *Acta Mater.* **2017**, *125*, 465.
[29] Y. Yao, Z. Huang, P. Xie, S. D. Lacey, R. J. Jacob, H. Xie, F. Chen, A. Nie, T. Pu, M. Rehwoldt, D. Yu, M. R. Zachariah, C. Wang, R. Shahbazian-Yassar, J. Li, L. Hu, *Science* **2018**, *359*, 1489.
[30] Y. Yao, Q. Dong, A. Brozena, J. Luo, J. Miao, M. Chi, C. Wang, I. G. Kevrekidis, Z. J. Ren, J. Greeley, G. Wang, A. Anapolsky, L. Hu, *Science* **2022**, *376*, eabn3103.
[31] T. Li, Y. Yao, B. H. Ko, Z. Huang, Q. Dong, J. Gao, W. Chen, J. Li, S. Li, X. Wang, R. Shahbazian-Yassar, F. Jiao, L. Hu, *Adv. Funct. Mater.* **2021**, *31*, 2010561.
[32] H. Zhu, S. Sun, J. Hao, Z. Zhuang, S. Zhang, T. Wang, Q. Kang, S. Lu, X. Wang, F. Lai, T. Liu, G. Gao, M. Du, D. Wang, *Energy Environ. Sci.* **2023**, *16*, 619.
[33] M. Cui, C. Yang, S. Hwang, M. Yang, S. Overa, Q. Dong, Y. Yao, A. H. Brozena, D. A. Cullen, M. Chi, T. F. Blum, D. Morris, Z. Finfrock, X. Wang, P. Zhang, V. G. Goncharov, X. Guo, J. Luo, Y. Mo, F. Jiao, L. Hu, *Sci. Adv.* **2022**, *8*, eabm4322.
[34] W. Zhu, J. Zhang, J. Luo, C. Zeng, H. Su, J. Zhang, R. Liu, E. Hu, Y. Liu, W. Liu, Y. Chen, W. Hu, Y. Xu, *Adv. Mater.* **2023**, *35*, 2208974.
[35] S. Liu, Z. Hu, Y. Wu, J. Zhang, Y. Zhang, B. Cui, C. Liu, S. Hu, N. Zhao, X. Han, A. Cao, Y. Chen, Y. Deng, W. Hu, *Adv. Mater.* **2020**, *32*, 2006034.
[36] Y. C. Han, M. L. Liu, L. Sun, S. Li, G. Li, W. S. Song, Y. J. Wang, Z. A. Nan, S. Y. Ding, H. G. Liao, Y. Yao, G. D. Stucky, F. R. Fan, Z. Q. Tian, *Proc. Natl. Acad. Sci* **2022**, *119*, 2121848119.
[37] C. Liu, Y. Shen, J. Zhang, G. Li, X. Zheng, X. Han, L. Xu, S. Zhu, Y. Chen, Y. Deng, W. Hu, *Adv. Energy Mater.* **2022**, *12*, 2103505.
[38] Y. Kang, A. Wang, R. Li, Y. Song, X. Wang, H. Li, W. Xu, L. Zhang, Q. Dong, *Adv. Mater.* **2022**, *34*, 2203166.
[39] S. Dou, J. Xu, X. Cui, W. Liu, Z. Zhang, Y. Deng, W. Hu, Y. Chen, *Adv. Energy Mater.* **2020**, *10*, 2001331.
[40] Y. Wu, Z. Zeng, S. Lei, M. Liu, W. Zhong, M. Qin, S. Cheng, J. Xie, *Angew. Chem., Int. Ed.* **2023**, *62*, 202217774.
[41] A. J. Martinolich, J. A. Kurzman, J. R. Neilson, *J. Am. Chem. Soc.* **2016**, *138*, 11031.
[42] Y. Zheng, Z. Yao, Z. Shadike, M. Lei, J. Liu, C. Li, *Adv. Funct. Mater.* **2022**, *32*, 2107060.
[43] P. Wei, J. Zhou, X. Pang, H. Liu, K. Deng, G. Wang, Y. Wu, B. Chen, *J. Mater. Chem. A* **2014**, *2*, 1128.
[44] A. Fuentes, *Solid State Ion.* **1997**, *93*, 245.
[45] Y. Yang, H. Zhu, F. Yang, F. Yang, D. Chen, Z. Wen, D. Wu, M. Ye, Y. Zhang, J. Zhao, Q. Liu, X. Lu, M. Gu, C. C. Li, W. He, *Nano Lett.* **2021**, *21*, 9675.

 © 2024 Wiley-VCH GmbH

16163028, 0, Downloaded from https://onlinelibrary.wiley.com/doi/10.1002/adfm.202315248 by Xiamen University, Wiley Online Library on [18/02/2024]. See the Terms and Conditions (https://onlinelibrary.wiley.com/terms-and-conditions) on Wiley Online Library for rules of use; OA articles are governed by the applicable Creative Commons License

[46] C. Guo, Z. Liu, K. Han, L. Zhang, X. Ding, X. Wang, L. Mai, *Small* **2022**, *18*, 2107365.
[47] X. Huang, W. Zhou, X. Chen, C. Jiang, Z. Zou, *Electrochim. Acta* **2021**, *368*, 137613.
[48] R. Tao, T. Zhang, S. Tan, C. J. Jafta, C. Li, J. Liang, X. Sun, T. Wang, J. Fan, Z. Lu, C. A. Bridges, X. Suo, C. Do-Thanh, S. Dai, *Adv. Energy Mater.* **2022**, *12*, 2200519.
[49] L. D. Salzer, B. Diamond, K. Nieto, R. C. Evans, A. L. Prieto, J. B. Sambur, *ACS Appl. Energy Mater.* **2023**, *6*, 1685.
[50] Y. Yang, H. Zhu, J. Xiao, H. Geng, Y. Zhang, J. Zhao, G. Li, X. Wang, C. C. Li, Q. Liu, *Adv. Mater.* **2020**, *32*, 1905295.
[51] N. G. Eror, U. Balachandran, *J. Solid State Chem.* **1982**, *45*, 276.
[52] L. Perfler, V. Kahlenberg, C. Wikete, D. Schmidmair, M. Tribus, R. Kaindl, *Inorg. Chem.* **2015**, *54*, 6836.
[53] A. A. Voskanyan, M. Abramchuk, A. Navrotsky, *Chem. Mater.* **2020**, *32*, 5301.
[54] X. Lu, Z. Jian, Z. Fang, L. Gu, Y.-S. Hu, W. Chen, Z. Wang, L. Chen, *Energy Environ. Sci.* **2011**, *4*, 2638.
[55] M. W. Logan, D. Zhang, B. Tan, K. Gerasopoulos, *J. Mater. Chem. A* **2021**, *9*, 11228.
[56] C. Yang, S. Deng, C. Lin, S. Lin, Y. Chen, J. Li, H. Wu, *Nanoscale* **2016**, *8*, 18792.
[57] T. Yuan, S. Luo, L. Soule, J.-H. Wang, Y. Wang, D. Sun, B. Zhao, W. Li, J. Yang, S. Zheng, M. Liu, *Mater. Today* **2021**, *45*, 8.
[58] X. Lou, R. Li, X. Zhu, L. Luo, Y. Chen, C. Lin, H. Li, X. S. Zhao, *ACS Appl. Mater. Interfaces* **2019**, *11*, 6089.
[59] A. Naik, J. Zhou, C. Gao, L. Wang, *Electrochim. Acta* **2014**, *142*, 215.
[60] Y. Liu, X. Yan, B. Xu, J. Lan, Y. Yu, X. Yang, Y. Lin, C. Nan, *Chem. Eng. J.* **2019**, *361*, 1371.
[61] Z. Yao, X. Xia, C. Zhou, Y. Zhong, Y. Wang, S. Deng, W. Wang, X. Wang, J. Tu, *Adv. Sci.* **2018**, *5*, 1700786.
[62] Z. Lv, H. Zhu, W. Meng, L. Wei, Y. Yang, Y. Zhang, M. Ye, C. C. Li, *Appl. Phys. Rev.* **2021**, *8*, 031404.
[63] H. Zhu, L. Yan, M. Xia, X. Cheng, W. Ye, H. Yu, N. Long, M. Shui, J. Shu, *J. Power Sources* **2019**, *426*, 250.
[64] X. Wang, C. Jaye, K. Nam, B. Zhang, H. Chen, J. Bai, H. Li, X. Huang, D. Fischer, X. Yang, *J. Mater. Chem. A* **2011**, *21*, 11406.
[65] R. Bernhard, S. Meini, H. A. Gasteiger, *J. Electrochem. Soc.* **2014**, *161*, A497.
[66] Y.-B. He, F. Ning, B. Li, Q.-S. Song, W. Lv, H. Du, D. Zhai, F. Su, Q.-H. Yang, F. Kang, *J. Power Sources* **2012**, *202*, 253.
[67] A. Du Pasquier, F. Disma, T. Bowmer, A. S. Gozdz, G. Amatucci, J.-M. Tarascon, *J. Electrochem. Soc.* **1998**, *145*, 1413.
[68] B. Zhao, X. Deng, R. Ran, M. Liu, Z. Shao, *Adv. Energy Mater.* **2016**, *6*, 1500924.
[69] T. Yokoshima, D. Mukoyama, F. Maeda, T. Osaka, K. Takazawa, S. Egusa, S. Naoi, S. Ishikura, K. Yamamoto, *J. Power Sources* **2018**, *393*, 67.
[70] J. Wang, W. Mei, Z. Cui, W. Shen, Q. Duan, Y. Jin, J. Nie, Y. Tian, Q. Wang, J. Sun, *Appl. Therm. Eng.* **2020**, *171*, 115082.
[71] R. Zhao, J. Liu, J. Gu, *Appl. Energy* **2016**, *173*, 29.

© 2024 Wiley-VCH GmbH

16163028, 0, Downloaded from https://onlinelibrary.wiley.com/doi/10.1002/adfm.202315248 by Xiamen University, Wiley Online Library on [18/02/2024]. See the Terms and Conditions (https://onlinelibrary.wiley.com/terms-and-conditions) on Wiley Online Library for rules of use; OA articles are governed by the applicable Creative Commons License